

Proceedings of the 12th International Conference on
Computational Fluid Dynamics in the Oil & Gas,
Metallurgical and Process Industries

Progress in Applied CFD – CFD2017



SINTEF Proceedings

Editors:

Jan Erik Olsen and Stein Tore Johansen

Progress in Applied CFD – CFD2017

Proceedings of the 12th International Conference on Computational Fluid Dynamics
in the Oil & Gas, Metallurgical and Process Industries

SINTEF Academic Press

SINTEF Proceedings no 2

Editors: Jan Erik Olsen and Stein Tore Johansen

Progress in Applied CFD – CFD2017

Selected papers from 10th International Conference on Computational Fluid Dynamics in the Oil & Gas, Metallurgical and Process Industries

Key words:

CFD, Flow, Modelling

Cover, illustration: Arun Kamath

ISSN 2387-4295 (online)

ISBN 978-82-536-1544-8 (pdf)

© Copyright SINTEF Academic Press 2017

The material in this publication is covered by the provisions of the Norwegian Copyright Act. Without any special agreement with SINTEF Academic Press, any copying and making available of the material is only allowed to the extent that this is permitted by law or allowed through an agreement with Kopinor, the Reproduction Rights Organisation for Norway. Any use contrary to legislation or an agreement may lead to a liability for damages and confiscation, and may be punished by fines or imprisonment

SINTEF Academic Press

Address: Forskningsveien 3 B
 PO Box 124 Blindern
 N-0314 OSLO

Tel: +47 73 59 30 00

Fax: +47 22 96 55 08

www.sintef.no/byggforsk

www.sintefbok.no

SINTEF Proceedings

SINTEF Proceedings is a serial publication for peer-reviewed conference proceedings on a variety of scientific topics.

The processes of peer-reviewing of papers published in SINTEF Proceedings are administered by the conference organizers and proceedings editors. Detailed procedures will vary according to custom and practice in each scientific community.

PREFACE

This book contains all manuscripts approved by the reviewers and the organizing committee of the 12th International Conference on Computational Fluid Dynamics in the Oil & Gas, Metallurgical and Process Industries. The conference was hosted by SINTEF in Trondheim in May/June 2017 and is also known as CFD2017 for short. The conference series was initiated by CSIRO and Phil Schwarz in 1997. So far the conference has been alternating between CSIRO in Melbourne and SINTEF in Trondheim. The conferences focuses on the application of CFD in the oil and gas industries, metal production, mineral processing, power generation, chemicals and other process industries. In addition pragmatic modelling concepts and bio-mechanical applications have become an important part of the conference. The papers in this book demonstrate the current progress in applied CFD.

The conference papers undergo a review process involving two experts. Only papers accepted by the reviewers are included in the proceedings. 108 contributions were presented at the conference together with six keynote presentations. A majority of these contributions are presented by their manuscript in this collection (a few were granted to present without an accompanying manuscript).

The organizing committee would like to thank everyone who has helped with review of manuscripts, all those who helped to promote the conference and all authors who have submitted scientific contributions. We are also grateful for the support from the conference sponsors: ANSYS, SFI Metal Production and NanoSim.

Stein Tore Johansen & Jan Erik Olsen



Organizing committee:

Conference chairman: Prof. Stein Tore Johansen

Conference coordinator: Dr. Jan Erik Olsen

Dr. Bernhard Müller

Dr. Sigrid Karstad Dahl

Dr. Shahriar Amini

Dr. Ernst Meese

Dr. Josip Zoric

Dr. Jannike Solsvik

Dr. Peter Witt

Scientific committee:

Stein Tore Johansen, SINTEF/NTNU

Bernhard Müller, NTNU

Phil Schwarz, CSIRO

Akio Tomiyama, Kobe University

Hans Kuipers, Eindhoven University of Technology

Jinghai Li, Chinese Academy of Science

Markus Braun, Ansys

Simon Lo, CD-adapco

Patrick Segers, Universiteit Gent

Jiyuan Tu, RMIT

Jos Derksen, University of Aberdeen

Dmitry Eskin, Schlumberger-Doll Research

Pär Jönsson, KTH

Stefan Pirker, Johannes Kepler University

Josip Zoric, SINTEF

CONTENTS

PRAGMATIC MODELLING	9
On pragmatism in industrial modeling. Part III: Application to operational drilling	11
CFD modeling of dynamic emulsion stability	23
Modelling of interaction between turbines and terrain wakes using pragmatic approach	29
FLUIDIZED BED	37
Simulation of chemical looping combustion process in a double looping fluidized bed reactor with cu-based oxygen carriers.....	39
Extremely fast simulations of heat transfer in fluidized beds.....	47
Mass transfer phenomena in fluidized beds with horizontally immersed membranes	53
A Two-Fluid model study of hydrogen production via water gas shift in fluidized bed membrane reactors	63
Effect of lift force on dense gas-fluidized beds of non-spherical particles	71
Experimental and numerical investigation of a bubbling dense gas-solid fluidized bed	81
Direct numerical simulation of the effective drag in gas-liquid-solid systems	89
A Lagrangian-Eulerian hybrid model for the simulation of direct reduction of iron ore in fluidized beds.....	97
High temperature fluidization - influence of inter-particle forces on fluidization behavior	107
Verification of filtered two fluid models for reactive gas-solid flows	115
BIOMECHANICS.....	123
A computational framework involving CFD and data mining tools for analyzing disease in carotid artery	125
Investigating the numerical parameter space for a stenosed patient-specific internal carotid artery model.....	133
Velocity profiles in a 2D model of the left ventricular outflow tract, pathological case study using PIV and CFD modeling.....	139
Oscillatory flow and mass transport in a coronary artery.....	147
Patient specific numerical simulation of flow in the human upper airways for assessing the effect of nasal surgery.....	153
CFD simulations of turbulent flow in the human upper airways	163
OIL & GAS APPLICATIONS	169
Estimation of flow rates and parameters in two-phase stratified and slug flow by an ensemble Kalman filter	171
Direct numerical simulation of proppant transport in a narrow channel for hydraulic fracturing application	179
Multiphase direct numerical simulations (DNS) of oil-water flows through homogeneous porous rocks	185
CFD erosion modelling of blind tees	191
Shape factors inclusion in a one-dimensional, transient two-fluid model for stratified and slug flow simulations in pipes	201
Gas-liquid two-phase flow behavior in terrain-inclined pipelines for wet natural gas transportation	207

NUMERICS, METHODS & CODE DEVELOPMENT	213
Innovative computing for industrially-relevant multiphase flows	215
Development of GPU parallel multiphase flow solver for turbulent slurry flows in cyclone.....	223
Immersed boundary method for the compressible Navier–Stokes equations using high order summation-by-parts difference operators	233
Direct numerical simulation of coupled heat and mass transfer in fluid-solid systems	243
A simulation concept for generic simulation of multi-material flow, using staggered Cartesian grids.....	253
A cartesian cut-cell method, based on formal volume averaging of mass, momentum equations.....	265
SOFT: a framework for semantic interoperability of scientific software	273
POPULATION BALANCE	279
Combined multifluid-population balance method for polydisperse multiphase flows	281
A multifluid-PBE model for a slurry bubble column with bubble size dependent velocity, weight fractions and temperature.....	285
CFD simulation of the droplet size distribution of liquid-liquid emulsions in stirred tank reactors	295
Towards a CFD model for boiling flows: validation of QMOM predictions with TOPFLOW experiments	301
Numerical simulations of turbulent liquid-liquid dispersions with quadrature-based moment methods.....	309
Simulation of dispersion of immiscible fluids in a turbulent couette flow	317
Simulation of gas-liquid flows in separators - a Lagrangian approach.....	325
CFD modelling to predict mass transfer in pulsed sieve plate extraction columns	335
BREAKUP & COALESCENCE	343
Experimental and numerical study on single droplet breakage in turbulent flow	345
Improved collision modelling for liquid metal droplets in a copper slag cleaning process	355
Modelling of bubble dynamics in slag during its hot stage engineering.....	365
Controlled coalescence with local front reconstruction method	373
BUBBLY FLOWS	381
Modelling of fluid dynamics, mass transfer and chemical reaction in bubbly flows	383
Stochastic DSMC model for large scale dense bubbly flows.....	391
On the surfacing mechanism of bubble plumes from subsea gas release.....	399
Bubble generated turbulence in two fluid simulation of bubbly flow	405
HEAT TRANSFER	413
CFD-simulation of boiling in a heated pipe including flow pattern transitions using a multi-field concept	415
The pear-shaped fate of an ice melting front	423
Flow dynamics studies for flexible operation of continuous casters (flow flex cc).....	431
An Euler-Euler model for gas-liquid flows in a coil wound heat exchanger.....	441
NON-NEWTONIAN FLOWS.....	449
Viscoelastic flow simulations in disordered porous media	451
Tire rubber extrudate swell simulation and verification with experiments	459
Front-tracking simulations of bubbles rising in non-Newtonian fluids.....	469
A 2D sediment bed morphodynamics model for turbulent, non-Newtonian, particle-loaded flows.....	479

METALLURGICAL APPLICATIONS.....	491
Experimental modelling of metallurgical processes	493
State of the art: macroscopic modelling approaches for the description of multiphysics phenomena within the electroslag remelting process	499
LES-VOF simulation of turbulent interfacial flow in the continuous casting mold	507
CFD-DEM modelling of blast furnace tapping	515
Multiphase flow modelling of furnace tapholes	521
Numerical predictions of the shape and size of the raceway zone in a blast furnace.....	531
Modelling and measurements in the aluminium industry - Where are the obstacles?	541
Modelling of chemical reactions in metallurgical processes.....	549
Using CFD analysis to optimise top submerged lance furnace geometries	555
Numerical analysis of the temperature distribution in a martensitic stainless steel strip during hardening.....	565
Validation of a rapid slag viscosity measurement by CFD.....	575
Solidification modeling with user defined function in ANSYS Fluent.....	583
Cleaning of polycyclic aromatic hydrocarbons (PAH) obtained from ferroalloys plant.....	587
Granular flow described by fictitious fluids: a suitable methodology for process simulations	593
A multiscale numerical approach of the dripping slag in the coke bed zone of a pilot scale Si-Mn furnace.....	599
INDUSTRIAL APPLICATIONS	605
Use of CFD as a design tool for a phosphoric acid plant cooling pond	607
Numerical evaluation of co-firing solid recovered fuel with petroleum coke in a cement rotary kiln: Influence of fuel moisture	613
Experimental and CFD investigation of fractal distributor on a novel plate and frame ion-exchanger	621
COMBUSTION	631
CFD modeling of a commercial-size circle-draft biomass gasifier.....	633
Numerical study of coal particle gasification up to Reynolds numbers of 1000.....	641
Modelling combustion of pulverized coal and alternative carbon materials in the blast furnace raceway	647
Combustion chamber scaling for energy recovery from furnace process gas: waste to value	657
PACKED BED.....	665
Comparison of particle-resolved direct numerical simulation and 1D modelling of catalytic reactions in a packed bed	667
Numerical investigation of particle types influence on packed bed adsorber behaviour	675
CFD based study of dense medium drum separation processes	683
A multi-domain 1D particle-reactor model for packed bed reactor applications.....	689
SPECIES TRANSPORT & INTERFACES	699
Modelling and numerical simulation of surface active species transport - reaction in welding processes	701
Multiscale approach to fully resolved boundary layers using adaptive grids.....	709
Implementation, demonstration and validation of a user-defined wall function for direct precipitation fouling in Ansys Fluent.....	717

FREE SURFACE FLOW & WAVES	727
Unresolved CFD-DEM in environmental engineering: submarine slope stability and other applications.....	729
Influence of the upstream cylinder and wave breaking point on the breaking wave forces on the downstream cylinder	735
Recent developments for the computation of the necessary submergence of pump intakes with free surfaces	743
Parallel multiphase flow software for solving the Navier-Stokes equations	752
 PARTICLE METHODS	 759
A numerical approach to model aggregate restructuring in shear flow using DEM in Lattice-Boltzmann simulations	761
Adaptive coarse-graining for large-scale DEM simulations.....	773
Novel efficient hybrid-DEM collision integration scheme.....	779
Implementing the kinetic theory of granular flows into the Lagrangian dense discrete phase model.....	785
Importance of the different fluid forces on particle dispersion in fluid phase resonance mixers	791
Large scale modelling of bubble formation and growth in a supersaturated liquid.....	798
 FUNDAMENTAL FLUID DYNAMICS	 807
Flow past a yawed cylinder of finite length using a fictitious domain method	809
A numerical evaluation of the effect of the electro-magnetic force on bubble flow in aluminium smelting process.....	819
A DNS study of droplet spreading and penetration on a porous medium.....	825
From linear to nonlinear: Transient growth in confined magnetohydrodynamic flows.....	831

IMPORTANCE OF THE DIFFERENT FLUID FORCES ON PARTICLE DISPERSION IN FLUID PHASE RESONANCE MIXERS

Silvio SCHMALFUSS^{1*}, Martin SOMMERFELD¹

¹ Otto-von-Guericke-University Magdeburg, 06130 Halle (Saale), GERMANY

* E-mail: silvio.schmalfuss@ovgu.de

ABSTRACT

In Fluid Phase Resonance (FPR) mixers, a central pipe reaches into the liquid phase inside a mixing vessel. Thus two closed gas cushions are formed above the liquid – one inside the pipe and one above the liquid inside the vessel. A drive attached at the top of the pipe creates low frequency (typically in a range from 1 s^{-1} to 5 s^{-1}) harmonical pressure oscillations in the gas cushion inside the pipe, which in turn induce a motion inside all the liquid in the vessel. This motion of the liquid is utilised for the purpose of mixing and dispersion of particles.

Simulations are performed for four different geometries of the central pipe's lower exit and for different particle Stokes numbers. Particle Stokes numbers are varied from $9.7 \cdot 10^{-4}$ to 2.7 by changing the particle diameter and density. The flow field inside the vessel was simulated with a Volume-of-Fluid solver to capture the free surface and the influence of the gas cushions, which act like springs, until a quasi-steady state was reached. One of these simulations was verified with Laser Doppler Anemometry measurements. For each simulation, the flow fields of the last full oscillation period are stored. The particles are then repeatedly tracked through these flow fields for 15 oscillations with an Euler-Lagrange approach with one-way-coupling, so that there is no need to recalculate the flow fields. The particles are considered as point masses, which are exposed to added mass, buoyancy, drag, gravity, history, pressure gradient, rotational lift, and shear lift force. Hydrodynamic torque is also considered, as well as a Langevin model for turbulent dispersion and a wall collision model accounting for rotation.

Mixing quality and time are determined by means of correlation dimension and the 90% lifting criterion whereby one of the four pipe exit configurations was identified as the best one. For this configuration two more oscillation frequencies are also investigated. Increasing the frequency to the resonance frequency leads to a more intense mixing process. Increasing it further drastically reduces the fluid velocity and deteriorates the mixing properties.

Furthermore, the influence of the different forces on the particles is investigated. The often neglected added mass and history forces are quite relevant for all particles investigated, having always more than 10% of the drag force's magnitude, with maximum values of up to 142% for added mass and up to 66% for history force. Pressure gradient force is highly relevant for larger particles. The rotational lift force is important for large particles only. Finally, the shear lift force is highly important, especially for larger and denser particle, but negligible for small, light particles.

Keywords: CFD, Euler-Lagrange, particle forces, LDA, mixing, Fluid Phase Resonance mixer.

NOMENCLATURE

Greek Symbols

ε	Turbulent dissipation rate, [m^2/s^3]
μ_F	Fluid dynamic viscosity, [$\text{kg}/(\text{m} \cdot \text{s})$]
ρ_F	Fluid density, [kg/m^3]
ρ_P	Particle density, [kg/m^3]
τ_F	Fluid time scale, [s]
τ_P	Particle time scale, [s]
ω	Turbulent frequency, [s^{-1}]

Latin Symbols

d_2	Correlation dimension, [-]
d_p	Particle diameter, [m]
f	Frequency, [s^{-1}]
F_{drag}	Drag force, [N]
\vec{F}_i	Force i, [N]
i	Index i, [-]
k	Turbulent kinetic energy, [m^2/s^2]
m_p	Particle mass, [kg]
P_2	Number of pairs, [-]
r	Distance, [m]
St	Stokes number, [-]
T	Oscillation period, [s]
t	Time, [s]
U	Velocity, [m/s]
u'	Turbulent velocity fluctuation, [m/s]
$U_{i,max/min}$	Max/min velocity in direction i, [m/s]
$U_{i,max/min,turb}$	Max/min velocity in direction i including turbulent fluctuation, [m/s]
\vec{u}_p	Particle velocity, [m/s]
\bar{U}_Z	Average velocity in axial direction, [m/s]
$U_{Z,max}$	Maximum velocity in axial direction, [m/s]
$U_{Z,min}$	Minimum velocity in axial direction, [m/s]
V	Volume, [m^3]
\vec{x}_p	Particle position, [m]

INTRODUCTION

FPR mixers are a comparatively new kind of mixing technology. Instead of a stirrer, here a central pipe reaches into a liquid contained in a mixing vessel. Two closed gas cushions are formed, one outside and one inside the central pipe. The latter is exposed to a harmonically oscillating pressure created by a drive attached to the central pipe, causing an oscillating movement of the liquid inside the pipe, which in turn induces a non-zero mean flow inside all the liquid as shown in Schmalfuß et al (2012). This flow is in this case utilised for the dispersion of solid particles. Usually, the oscillation frequencies are in a range between 1 s^{-1} and 5 s^{-1} . According to Schmalfuß and Sommerfeld (2017) the flow properties and therefore also the mixing properties (e.g. velocity magnitude, turbulence, structure) are mainly defined by the central pipe's geometry and the oscillating frequency. On the one hand, this work investigates these influences to improve the mixing quality of FPR mixers. On the other hand, also the influence of different forces acting on the particles is analysed. Considered forces are drag force, added mass force, Basset force (or history force), pressure gradient force, gravity force including buoyancy, and the transverse lift forces due to shear and rotational lift. Some of these forces are usually neglected when it comes to the simulation of industrial scale processes, especially added mass and Basset force. The present work shall reveal if this practice is justified.

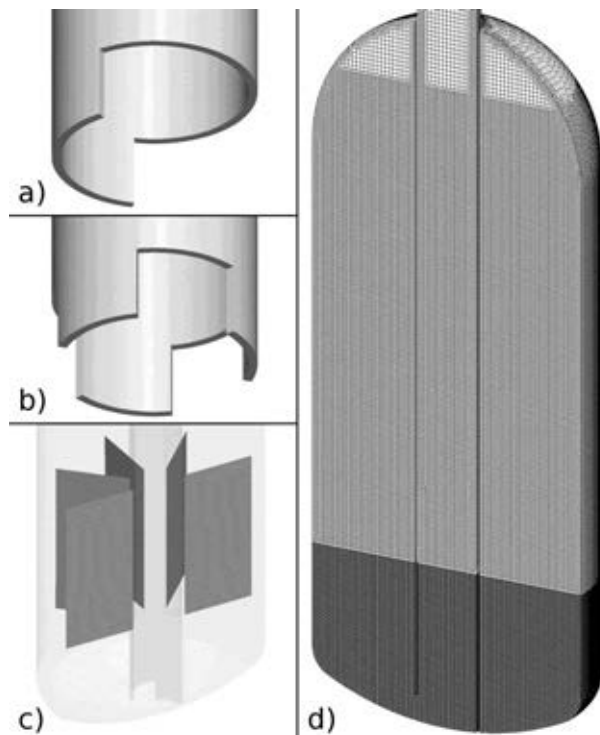


Figure 1: Geometry and computational domain; a) one-sided cutout pipe end; b) tripod pipe end; c) measurement planes (left: 0° , right: 180°); d) computational grid.

GEOMETRY AND PROCESS PARAMETERS

A vessel with a torispherical bottom is used as mixing vessel. Its geometrical properties are summarised in Table 1 and the different central pipe ends are shown in Figure 1 a) and b). Having a diameter of 0.45 m and a

filling height of 0.7 m results in a filling-height to diameter ratio of ~ 1.6 . The first pipe end is a 225° -cutout, leaving a kind of nose at the end of the pipe and it will be referred to as “one-sided cutout”. The second pipe end consists of three 60° -cutouts, resulting in a tripod-like shape with three 60° -noses, henceforth referred to as “tripod”. Both central pipes have an inner diameter of 0.1 m. For each pipe two different mounting heights are considered. One time the pipe ends directly at the vessel bottom, leaving only small gaps at the cutouts, the other time the pipe is lifted by 20 mm. These two pipe heights will be referred to as “at bottom” or “lifted”, respectively. The drive frequency is 1.2 s^{-1} for all configurations. For the configuration “tripod at bottom” two higher frequencies, namely 1.5 s^{-1} and 2.0 s^{-1} , are used to investigate the frequency's influence. Water and air at room temperature and ambient pressure are used as the two phases. Their properties are listed in Table 2. The particles have densities of 1050 kg/m^3 , 1500 kg/m^3 , and 2500 kg/m^3 . Their diameters are $80 \mu\text{m}$, $500 \mu\text{m}$, $1500 \mu\text{m}$, and $2500 \mu\text{m}$.

Table 1: Geometry parameters.

Pipe		At bottom	Lifted
Vessel diameter	[m]	0.45	
Vessel height	[m]	1.1	
Filling height	[m]	0.70	
Pipe diameter	[m]	0.1	
Pipe height	[m]	-	0.020
Cutout height	[m]	0.04	

Table 2: Fluid phase material parameters.

		Water	Air
Density	$[\text{kg/m}^3]$	1000	1.3
Kinematic viscosity	$[\text{m}^2/\text{s}]$	$1 \cdot 10^{-6}$	$13 \cdot 10^{-6}$
Compressibility	$[\text{s}^2/\text{m}^2]$	$4.7 \cdot 10^{-10}$	$9.9 \cdot 10^{-6}$
Surface tension	$[\text{kg/s}^2]$	0.073	

NUMERICAL AND EXPERIMENTAL METHODS

Fluid flow

The fluid flow is simulated as an unsteady, compressible flow of two separate phases, namely water and air. OpenFOAM's solver compressibleInterFoam, employing a Volume-of-Fluid approach with interface compression, is used for this task. The geometries are discretised into approximately 4 million cells, whereby a symmetry plane is used as shown in Figure 1d) to lower the requirements on computational resources. At the top of the central pipe, a harmonically oscillating velocity normal to the surface is used as boundary condition, according to the parameters given by the drive attached to the pipe. At the symmetry plane a symmetry boundary condition is used and at the walls a no-slip condition is applied. Previous simulations by Schmalfuß et al (2012) have shown that the $k-\omega$ -SST turbulence model gives the best results compared to

others. Thus, it is also used here. To ensure a quasi-steady flow, where after one oscillation the same flow field is found again, the flow is simulated for 20 periods. The averaged velocity components for the simulations are the arithmetic means of the three velocity components or the velocity magnitude, respectively, over the time of one period at the end of the simulation. Maximum and minimum velocities $U_{i,max/min,turb}$ in directions i are calculated with the corresponding velocities during the analysed time period and the turbulent velocity fluctuations u' , which are estimated from turbulent kinetic energy k , assuming isotropic turbulence:

$$U_{i,max/min,turb} = U_{i,max/min} \pm u' = U_{i,max/min} \pm \sqrt{\frac{2}{3}k} \quad (1)$$

As another means of comparison between the configurations, the temporally and spatially averaged values of the turbulent kinetic energy and dissipation rate ε inside the liquid phase have been calculated.

The results of the flow field simulations are also used to calculate the turbulence characteristic time scale τ_F of the fluid as a temporally and spatially averaged value of the ratio of turbulent kinetic energy and turbulent dissipation rate:

$$\tau_F = \frac{1}{T} \int_t^{t+T} \frac{1}{V} \int_V \frac{k}{\varepsilon} dV dt \quad (2)$$

The temporal averaging is done over one oscillation period with duration T starting at time t , and the spatial averaging is done over the total liquid volume V .

Measurements with a one component Laser Doppler Anemometer (LDA) have been conducted in five planes for the configuration “one-sided cutout at bottom” to verify the simulations. The measurement planes can be seen in Figure 1c). There are two planes in the symmetry plane (one on each side of the pipe) and three planes between those two, each shifted by 45°. In each plane there are 156 measurement points, where axial and radial velocity components have been measured. Unfortunately, the tangential velocity component could not be measured in this geometry. Tracer particles with a diameter of 40 μm and a density of 1050 kg/m^3 are used. For LDA measurements it is important that these tracer particles follow the flow largely without slip, which means the particle Stokes number should be considerably below unity. Schmalfuß et al. (2012) have shown that the highest particle Stokes number occurs only in a very small region at the lower end of the immersed pipe with a value of about 0.14. Hence, the tracer particles should follow the flow to a large extent. In each measurement location 3000 Doppler signals are collected and statistically analysed. For the comparison of measurements and calculations, three different values are used: average, maximum and minimum velocities. The maximum and minimum velocities are determined for each point by the 0.05- or 0.95-quantile, respectively, of the 3000 values collected per point. The average is determined by an arrival time weighted average.

Particle motion and mixing properties

An Euler-Lagrange approach, where particles are treated as point masses, is used to calculate the particle behaviour. The flow field for these calculations is taken

from the flow simulations described above. For the last oscillation, the transient flow field is stored with a time step of 0.01 s. The particles are repeatedly tracked through these stored flow fields. After one oscillation the flow field states are used again. Of course, with this approach only one-way-coupling is possible, meaning that the particles do not have any influence on the flow field, implying that for the moment only low particle concentrations are considered. Consequently inter-particle collisions are also neglected. As a Lagrangian approach is used, the particle motion is calculated by:

$$\frac{d\vec{x}_p}{dt} = \vec{u}_p \quad (3)$$

$$\frac{d\vec{x}_p}{dt} m_p = \sum_i \vec{F}_i \quad (4)$$

Here, u_p and m_p are the particle velocity and mass, t is the time and F_i are the forces acting on the particle. The forces considered are added mass force, Basset force (also called history force), drag force, gravity and buoyancy force, pressure gradient force, and the transverse lift forces due to rotational and shear slip, see e.g. Sommerfeld et al (2008) or Crowe et al (2012). Shear lift is modelled according to the findings of Mei (1992) and rotational lift according to Oesterlé and Bui Dinh (1998). Added mass and Basset force are implemented according to Michaelides and Roig (2011). For the Basset force, the approximation of Hinsberg et al (2011) is used for solving the integro-differential equation. Otherwise, either the tail in Basset force calculation would have to be truncated or its calculation would lead to all but impossibly high needs in computational resources.

Additionally, the hydrodynamic torque is considered. It is calculated with correlations taken from Sommerfeld et al. (2008), which are based on experiments by Dennis et al. (1980) and Sawatzki (1970).

Wall collisions account for kinetic energy loss and friction and can alter the angular velocity of the particles, as described by Decker (2005).

The fluctuating velocities due to turbulence are not resolved when a RANS-model, like k- ω -SST in this case, is used to describe the turbulence. To model the turbulent velocity fluctuations seen by the particles, a single-step Langevin dispersion model is employed, as suggested by Sommerfeld et al. (1993).

At the beginning of the particle simulations, approximately 100,000 particles are randomly distributed near the bottom of the vessel with a velocity magnitude of zero. These particles are then, as described above, repeatedly tracked through the oscillating flow fields for 15 periods, which corresponds to a time of 12.5 s for the cases with $f = 1.2 \text{ s}^{-1}$.

The mixing properties are investigated using two parameters, namely mixing time and mixing quality. To judge about the mixing speed, the mixing time is defined as the 90% lifting criterion. This criterion is fulfilled as soon as the first particle reaches a height corresponding to 90% of the filling level. The mixing quality is investigated by means of the correlation dimension, which indicates how well the particle positions represent a random three dimensional distribution. Its values can vary between unity, representing a one-dimensional distribution, e.g. along a

line, and three, representing a random three dimensional distribution, e.g. in a spherical arrangement. The correlation dimension d_2 is temporally averaged over the last oscillation period and is calculated as:

$$d_2(r) = \lim_{r \rightarrow 0} \frac{d \ln P_2(r)}{d \ln r} \quad (5)$$

with $P_2(r)$ being the number of particle pairs closer than distance r to each other.

Influence of the different particle forces

The magnitude of all the forces acting on the particles is stored every 0.001 s for the last two oscillation periods. To analyse their influence, the values are averaged over the above mentioned last two periods and then normalised with the magnitude of the drag force. An averaged particle Stokes number is used as parameter for judging on the influence of the forces. This number describes the ability of the particles to follow the flow field and is defined as:

$$St = \frac{\tau_P}{\tau_F} \quad (6)$$

The fluid time scale τ_F has already been described above and is an average turbulence time scale in the entire liquid region. The Stokesian particle response time is

$$\tau_P = \frac{(\rho_P + 0.5\rho_F)d_P^2}{18\mu_F} \quad (7)$$

with μ_F and ρ_F being the dynamic viscosity and density of the fluid and ρ_P the particle density.

RESULTS

Fluid flow

The configuration “one-sided cutout at bottom” is also investigated by means of LDA. In Figure 2 the average, maximum, and minimum values of the vertical velocities in the five planes depicted in Figure 1c) are compared. In general, the comparison between measurement and simulation shows good agreement. Discrepancies can be seen especially at the 180° plane. This might be because this is the symmetry plane in the simulation, so there is a zero velocity imposed perpendicular to that plane, which in turn might cause higher flow rates in the directions parallel to the symmetry plane. In reality, of course, this is not the case. Furthermore, the extremal values are not always met in the measured observations compared to the numerical computations. This could be caused by the comparatively coarse measurement grid.

In Figure 3 the temporal averaged velocity magnitude, turbulent kinetic energy, and turbulent dissipation rate in the symmetry plane of the four configurations are compared. Regarding the velocities it can be seen that the highest values occur inside the pipe. A lifted central pipe results in higher velocities inside, but lower velocities outside the pipe. With a pipe at the bottom, there is a large region with high velocities at the vessel wall opposite the opening of the pipe for both, one-sided cutout and tripod. For a lifted pipe with the one-sided cutout, this region is considerably smaller and for the lifted tripod it is even at the opposite side. The pipe exit geometry seems to have only low influence on the velocity magnitude.

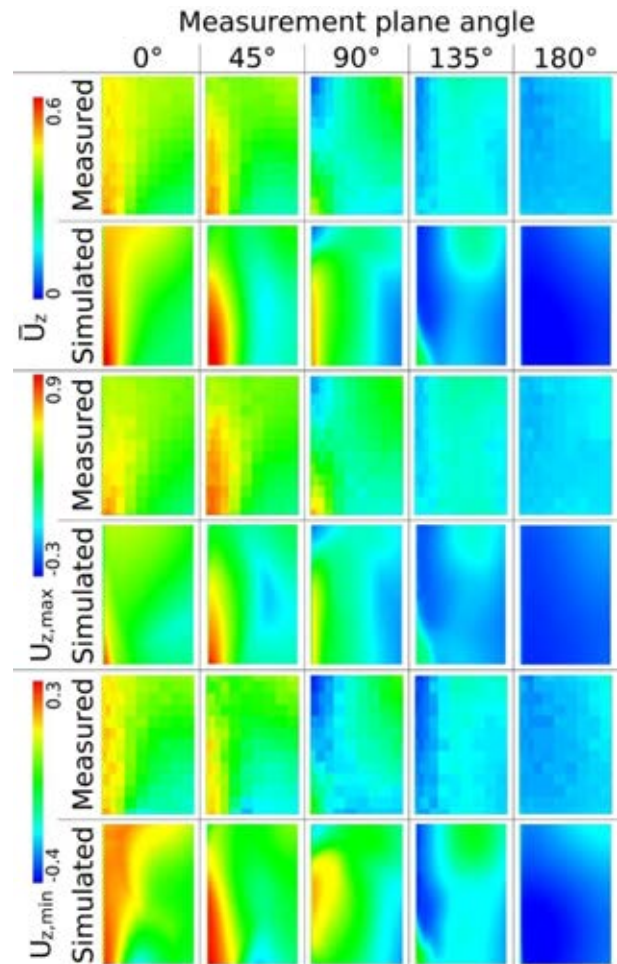


Figure 2: Comparison of temporal average, maximum, and minimum values of measured and calculated velocities (m/s) in axial direction in the measurement planes shown in Fig. 1c), for “one-sided cutout at bottom”.

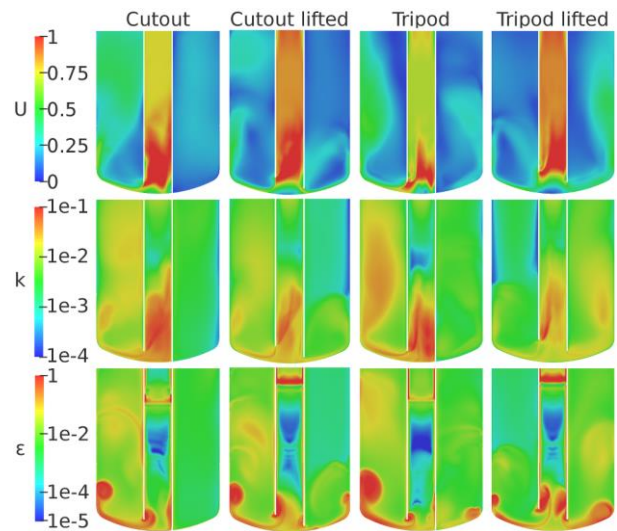


Figure 3: Comparison of temporal averaged values of velocity magnitude U in m/s, turbulent kinetic energy k in m^2/s^2 , and dissipation rate ε in m^2/s^3 for the different configurations in the symmetry plane

Turbulent kinetic energy k has its highest values inside the pipe near the pipe exit. With a pipe at the bottom, it has the same pattern for one-sided cutout and tripod, but it is higher for the tripod in most regions. Similar to the velocities, the lifted pipe versions show lower values

outside the pipe and for the lifted tripod a reversed left-to-right image with high values at the right vessel wall. Contrary to the findings for the velocities, the turbulent kinetic energy inside the pipe is higher for the pipe-at-bottom configurations. Overall it seems that k is higher for the versions with a pipe at the bottom.

Comparing the dissipation rate between the two one-sided cutout versions reveals that lifting the pipe leads to higher dissipation at the right side of the bottom. In the upper parts of the symmetry plane the dissipation rate seems to be almost the same for these two versions. The tripod at bottom has much larger regions with high dissipation rates than a one-sided cutout opposite to the pipe opening. Additionally there is also a region with high dissipation rates at the right side of the bottom. This region even increases for the version with the lifted tripod. But here the dissipation rate at the left side is significantly lower.

Figure 4 shows the influence of the drive's frequency on velocity, turbulent kinetic energy and dissipation rate. Increasing the frequency from 1.2 s^{-1} to 1.5 s^{-1} significantly increases all three quantities. This is because 1.5 s^{-1} is the resonance frequency of the system and so the movement of the liquid is the most intense. The higher velocities lead in turn to higher turbulence and thus to higher turbulent kinetic energy and dissipation rates. Increasing the frequency further to 2.0 s^{-1} , which means to a value clearly above the resonance frequency, leads to a heavy drop in all of the three quantities. This is because the oscillating system now cannot follow the excitation from the drive because it is too inertial.

Particle motion and mixing properties

Figure 5 shows exemplary results for the frozen particle positions after 15 oscillations in the "lifted tripod" configuration for particles with a density of 1500 kg/m^3 and with diameters from $80 \mu\text{m}$ to $2500 \mu\text{m}$, leading to Stokes numbers of 0.0013 to 1.2. The particles are colour coded by particle velocity magnitude. Unsurprisingly, the particles with low Stokes numbers seem to be distributed quite uniformly, whereas the more inertial particles tend to remain in the lower parts of the vessel, hence dispersion is not sufficient.

The relative mixing times, i.e. the times to fulfil the 90% lifting criterion normalised with the period duration, are shown in Table 3. Where no value is given, the criterion was not fulfilled. Considering only the configurations with an oscillation of $f = 1.2 \text{ s}^{-1}$, the "tripod at bottom" configuration reveals the best mixing speed for most of the investigated particle properties, which is why this configuration was also analysed at other frequencies. Only for particles having a diameter of $2500 \mu\text{m}$ and a density of 2500 kg/m^3 another configuration, namely the "one-sided cutout at bottom", has a shorter mixing time than the "tripod at bottom".

Raising the frequency to 1.5 s^{-1} gives even faster mixing speeds. This is due to the higher fluid velocities in the vessel. Due to resonance, the decrease in mixing time seems to be not linear, otherwise the relative mixing time should have been the same as for the lower frequency. Apparently, this is also the case when increasing the frequency above the resonance frequency, but here the relative mixing time rapidly

increases. This fits the observation of low velocities in the fluid flow simulations.

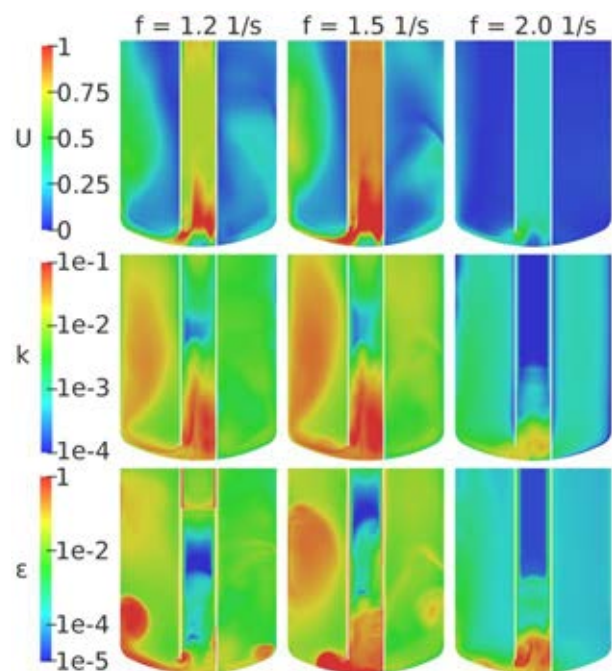


Figure 4: Influence of frequency on temporal averaged values of velocity magnitude U in m/s , turbulent kinetic energy k in m^2/s^2 , and dissipation rate ϵ in m^2/s^3 in the symmetry plane for "tripod at bottom".

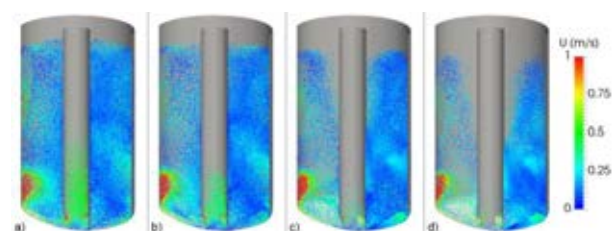


Figure 5: 3-dimensional view of particle positions and velocities at the end of 15 oscillations in the "tripod at bottom" with $\rho_p = 1500 \text{ kg/m}^3$; a) $d_p = 80 \mu\text{m}$, $St = 0.0013$, $d_2 = 2.84$; b) $d_p = 500 \mu\text{m}$, $St = 0.049$, $d_2 = 2.20$; c) $d_p = 1500 \mu\text{m}$, $St = 0.44$, $d_2 = 2.07$; d) $d_p = 2500 \mu\text{m}$, $St = 1.2$, $d_2 = 2.05$.

Table 4 lists the correlation dimensions at the end of the simulations for all considered particles. As might be expected, the correlation dimensions tend to lower values for higher particle diameters and densities. But there are some discrepancies to this overall trend. For example d_2 rises in the "one-sided cutout at bottom" and the "lifted tripod" when increasing the particle diameter from $1500 \mu\text{m}$ to $2500 \mu\text{m}$ for a particle density of 2500 kg/m^3 . This might be due to the fact that the correlation dimension does not account for the distribution of particles in the liquid volume, but only gives an estimate of how the particles are distributed at their locations. So for the large, heavy particles this means that they are quite randomly distributed, but only in a small region at the lower part of the vessel. The standard deviation of the particle concentration would prevent this drawback, but the particle concentrations considered are too small to provide sufficient information in every computational cell. Despite this, the d_2 -values indicate two configurations for best mixing, namely "tripod at bottom" for small and light particles and "lifted one-

sided cutout” for larger and heavier particles. Overall, the “tripod at bottom”-configuration seems to offer the best combination of mixing speed and quality.

Table 3: Relative mixing times for all simulations; bold letters denote the fastest mixing time for $f = 1.2 \text{ s}^{-1}$.

ρ_p [kg/m ³]	d_p [μm]	One-sided cutout at bottom	One-sided cutout lifted	Tripod at bottom	Tripod lifted	Tripod at bottom $f = 1.5 \text{ s}^{-1}$	Tripod at bottom $f = 2.0 \text{ s}^{-1}$
1050	80	1.2	1.3	1.2	1.2	0.90	5.6
	500	1.3	1.7	1.1	1.6	0.86	5.7
	1500	1.3	1.7	1.1	1.3	0.81	6.7
	2500	1.3	1.7	1.0	1.3	0.81	8.3
1500	80	1.2	1.3	1.1	1.2	0.84	5.6
	500	1.3	1.7	1.2	1.7	0.83	7.2
	1500	1.3	2.0	1.1	2.3	0.90	-
	2500	1.3	3.8	1.3	1.3	0.95	-
2500	80	1.3	1.3	1.1	1.2	0.86	5.6
	500	1.3	1.8	1.2	1.9	0.83	-
	1500	1.8	-	1.5	-	1.1	-
	2500	2.3	-	3.7	-	1.3	-

Table 4: Correlation dimensions for all simulations; bold letters denote the best (i.e. highest) values for $f = 1.2 \text{ s}^{-1}$.

ρ_p [kg/m ³]	d_p [μm]	One-sided cutout at bottom	One-sided cutout lifted	Tripod at bottom	Tripod lifted	Tripod at bottom $f = 1.5 \text{ s}^{-1}$	Tripod at bottom $f = 2.0 \text{ s}^{-1}$
1050	80	2.79	2.80	2.84	2.77	2.81	2.70
	500	2.63	2.74	2.79	2.74	2.78	2.44
	1500	2.24	2.75	2.75	2.73	2.77	1.91
	2500	2.18	2.76	2.75	2.72	2.77	1.64
1500	80	2.78	2.81	2.84	2.78	2.81	2.67
	500	1.52	2.76	2.20	2.73	2.37	1.70
	1500	1.30	2.65	2.07	2.10	1.78	1.46
	2500	1.48	2.47	2.05	1.74	1.61	2.24
2500	80	2.70	2.80	2.85	2.80	2.80	2.42
	500	1.82	2.37	1.66	1.97	1.77	1.56
	1500	1.42	2.36	1.91	1.94	1.74	2.13
	2500	1.58	1.76	1.72	2.19	1.82	1.80

Influence of the different particle forces

The influence of the different forces acting on particles with different Stokes numbers is shown in the graphs in Figure 6 for fixed particle densities. These values are averaged over all particles during the last two oscillation periods over all configurations with oscillation frequency $f = 1.2 \text{ s}^{-1}$, and afterwards the averages are normalised with regard to the average drag force magnitude. At small Stokes numbers the Basset force is the most important force after the drag force. It can be seen that the Basset force decreases with increasing diameter or Stokes number, respectively, whereas all other forces increase. This might be due to the circumstance that the Basset force tail is “deleted” when a particle hits a wall. Usually, more inertial particles are more likely to collide with walls than particles that

mainly follow the fluid flow. For higher Stokes numbers, all forces seem to have an influence on the particles with magnitudes of more than 10% of the drag force. For small Stokes numbers, some forces are relatively unimportant, namely pressure gradient and the two lift forces. For density ratios near unity, even the gravity and buoyancy force becomes negligible, leaving added mass and Basset force as the only two forces beneath drag force with a considerable contribution to the particle motion.

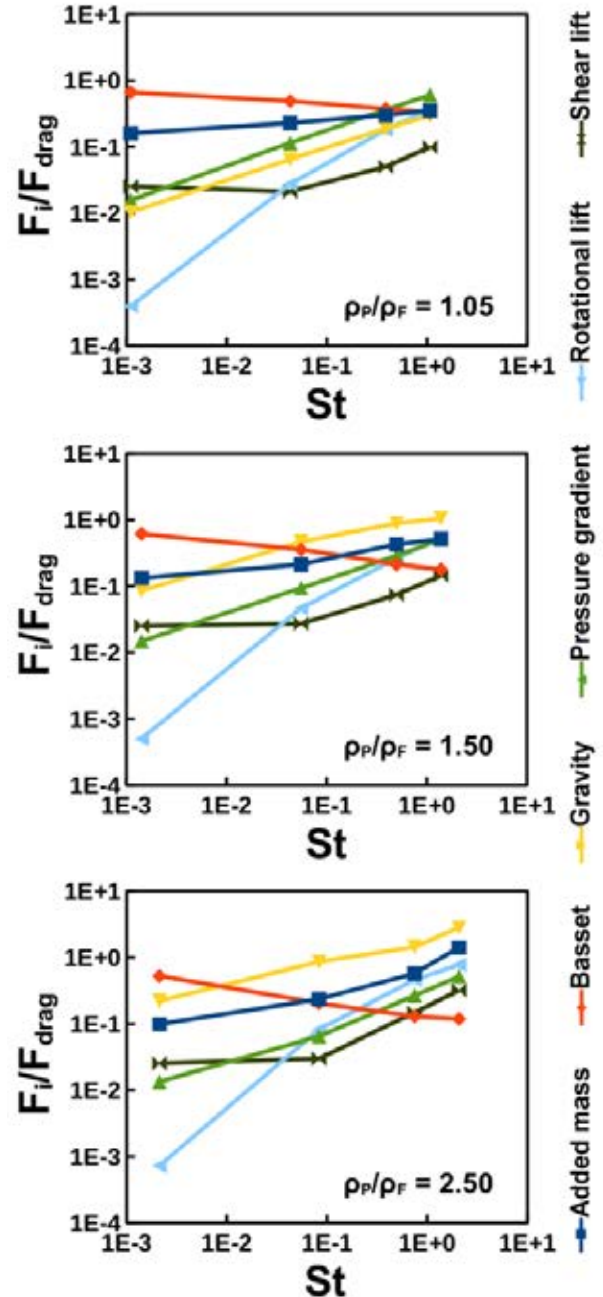


Figure 6: Averaged magnitude of considered forces F_i normalised by drag force F_{drag} for fixed density ratios ρ_p/ρ_F in dependence of particle Stokes number St .

Especially the fact that the magnitudes of added mass and Basset force are always higher than 10% of the drag force's magnitude should be emphasised. Due to their comparatively high demands for computational resources, these two forces are mostly neglected in particle simulations for industrial liquid-solid

multiphase flows like in mixing vessels. This is in this case clearly not justified. The same holds true for the two lift forces at higher Stokes number, meaning particles with large diameters or high density ratios. But it should be noted that this statement should be verified for other processes, as the flow in the FPR mixers is not necessarily comparable to flows in standard stirred vessels. On the other hand, in a stirred vessel the flow is much more inhomogeneous so that unsteady forces and the lift forces should be even more important.

CONCLUSIONS AND OUTLOOK

The fluid-flow simulation of FPR mixing vessels has been done and was verified with LDA measurements.

Regarding the influence of pipe geometry the conclusions are that lifting the pipe has a much larger influence on the flow than changing its exit geometry.

Furthermore, the oscillation frequency seems to have even more influence. Increasing it from a low frequency to the system's resonance frequency leads to a much more intense flow with higher velocities and higher turbulent kinetic energy and dissipation rates.

However, increasing the frequency further, above the resonance frequency, drastically decreases the velocities and the turbulence properties.

Several particle simulations have been done with the calculated flow fields, covering Stokes numbers from $9.7 \cdot 10^{-4}$ to 2.7. Mixing speed and mixing quality have been determined by means of the 90% lifting criterion and the correlation dimension. Overall the configuration "tripod at bottom" seems to have the best combination of mixing time and quality, even though the mixing quality of the "lifted one-sided cutout" is better for more inertial particles.

Eventually, the influence of the different particle forces considered has been investigated. The magnitudes of the often neglected added mass force and Basset force are always higher than 10% of the drag force's magnitude and reach values of 142% regarding added mass force, and 66% regarding Basset force. The lift forces are quite low for small Stokes numbers, but are not negligible for higher Stokes numbers. Summing up, it should not be taken for granted that neglecting all these forces is always justified.

The particle simulations are not verified yet, so measurements, e.g. with particle image velocimetry should be done. Additionally, the simulations could be improved, for example by including particle collisions, as suggested by Sommerfeld and Decker (2004), at least for high Stokes numbers, which lead to high particle concentrations at the bottom, or by extending the simulations to a fully 3-dimensional domain without a symmetry plane.

The different forces naturally strongly depend on the fluid flow and the flow inside FPR mixing vessels surely differs from flows obtained with standard stirrers. This holds true even more for flows in other processes. Thus, the statements about the influence of the forces should also be investigated for other stirrers and industry scale processes.

REFERENCES

- CROWE, C., SCHWARZKOPF, J.D., SOMMERFELD, M. and TSUJI, Y., (2012), "Multiphase Flow with Droplets and Particles", 2nd Edition, *CRC Press*, Boca Raton, ISBN: 978-1-4398-4050-4.
- DECKER, S., (2005), "Zur Berechnung von gerührten Suspensionen mit dem Euler-Lagrange-Verfahren", PhD-Thesis, Martin-Luther-University Halle (Saale) (Germany).
- DENNIS, S.C.R., SINGH, S.N., INGHAM, D.B., (1980), "The steady flow due to a rotating sphere at low and moderate Reynolds numbers", *J. Fluid Mech.*, **101**, 257-279.
- VAN HINSBERG, M.A.T., TEN THIJE BOONKAMP, J.H.M. and CLERCX, H.J.H., (2011), "An efficient, second order method for the approximation of the Basset history force", *J. Comp. Phys.*, **230**, 1465-1478.
- MEI, R., (1992), "An approximate expression for the shear lift force on a spherical particle at finite Reynolds number", *Int. J. Multiph. Flow*, **18**, 145-147.
- MICHAELIDES, E.E. and ROIG, A., (2011), "A reinterpretation of the Odar and Hamilton data on the unsteady equation of motion of particles", *AIChE J.*, **57**, 2997-3002.
- OESTERLÉ, B. and BUI DINH, T., (1998), "Experiments on the lift of a spinning sphere in a range of intermediate Reynolds numbers", *Exp. Fluids*, **25**, 16-22.
- SAWATZKI, O., (1980), „Über den Einfluß der Rotation und der Wandstöße auf die Flugbahn kugelig Teilchen im Luftstrom“, PhD-Thesis, University Karlsruhe (Germany).
- SCHMALFUSS, S., SÄUBERLICH, R. and SOMMERFELD, M., (2012), "CFD-Simulation und LDA-Messung der Strömungsvorgänge beim Fluidphasenresonanzmischen", *Chem. Ing. Tech.*, **84**, 547-552.
- SCHMALFUSS, S. and SOMMERFELD, M., (2017), "Numerical and experimental analysis of Fluid Phase Resonance mixers", *submitted to Chem. Eng. Sci.*
- SOMMERFELD, M. and DECKER, S., (2004), "State of the Art and Future Trends in CFD Simulation of Stirred Vessel Hydrodynamics", *Chem. Eng. Technol.*, **27**, 215-224.
- SOMMERFELD, M., KOHNEN, G. and RÜGER, M., (1993), „Some open questions and inconsistencies of Lagrangian particle dispersion models“, *Proceedings Ninth Symposium on Turbulent Shear Flows*, Kyoto (Japan), Paper No. 15-1.
- SOMMERFELD, M., VAN WACHEM, B., OLIEMANS, R., (2008), "Best Practice Guidelines for Computational Fluid Dynamics of Dispersed Multiphase Flows", ERCOFTAC (European Research Community on Flow, Turbulence and Combustion), ISBN 978-91-633-3564-8.